Performance and failure modes of mass timber buckling-restrained braces under cyclic loading

Toru Takeuchi [a],[*], Yuki Terazawa [a], Shogo Komuro [a], Takashi Kurata [b], Ben Sitler [b]

[a] *Tokyo Institute of Technology, Department of Architecture and Building Engineering, Ookayama 2-12-, Meguro-ku, Tokyo 152-8550, Japan*
[b] *Nippon Steel Engineering, Ohsaki 1-5-1, Shinagawa-ku, Tokyo 141-8604, Japan*

ARTICLE INFO

ABSTRACT

Buckling-restrained braces with mass timber restrainers (MT-BRBs) have recently been investigated by several researchers. However, timber restrainers exhibit brittle failure modes and have lower stiffness and strength than their composite and steel counterparts. Previous experiments have demonstrated that timber restrainers are particularly susceptible to local bulging and that this is a brittle failure resulting in a near total loss of strength. Nevertheless, local bulging and global stability design methods have not yet been established for BRBs with timber restrainers. This paper presents cyclic loading tests of MT-BRBs featuring different bolted restrainer compositions, core plate clearances, reinforcing plate arrangements, connections and boundary conditions. These tests produced a variety of weak- and strong-axis bulging and global buckling failure modes. Design methods were developed to prevent each failure mode and then used to design full-scale MT-BRBs that were successfully tested and exhibited excellent performance.

1. Introduction

Timber has recently been employed as a primary structural material to help reduce the carbon footprint of a wide variety of buildings. Engineered mass timber products such as glued laminated timber (glulam), laminated veneer lumber (LVL) and cross laminated timber (CLT) have featured prominently in these structures and have enabled increasingly large multi-story buildings [1]. However, heavy timber poses challenges for seismic applications, as timber beam-column connections tend to be flexible, while timber braces and shear walls exhibit less ductility than their steel and reinforced concrete counterparts. To overcome these shortcomings, researchers have proposed hybrid structures that combine timber gravity frames with ductile steel buckling-restrained braces (BRBs), steel shear links or steel reduced beam sections [2-4]. BRBs are particularly effective in enhancing the stiffness and energy-dissipation of mass timber frames and have been successfully tested in a glulam frame [5].

Mass timber has also been directly employed as the primary BRB restrainer material in lieu of mortar and steel. The potential advantages of timber include the elimination of wet trades during fabrication of the BRB and a more consistent visual aesthetic, as well as small reductions in the carbon footprint (braces comprise a small percentage of the total

structural volume) and lifting weight (BRB restrainers are ultimately governed by stiffness). Early tests by Yamada et.al [6] of BRBs with cedar or douglas fir infilled steel tube restrainers observed significantly degraded compressive behavior due to the low cross-grain strength of the timber. However, these specimens featured 2 mm debonding gaps, which were excessively thick for the 12 mm core plates, while the encasing steel tubes enhanced the behavior after the timber failed, maintaining some residual strength. Blomgren et al. [7] conducted uniaxial cyclic tests of BRBs with steel core plates sandwiched inside glulam restrainers, which featured two timber pieces joined with screws and steel plates to reinforce the timber in the core's strong axis. One specimen failed due to local bulging, while another achieved a stable hysteresis up to 1.16% average axial strain, but the method used to design the restrainer was not described. Resta [8] tested timber BRBs with steel core plates and reinforcing steel plates, but the lack of stiffeners at the restrainer end resulted in unstable hysteresis loops with local and global out-of-plane buckling. Murphy et al. [9] tested 5 timber BRB specimens featuring steel core plates sandwiched between bolted mass plywood panels with hardwood spacers. These were some of the most successful tests conducted to date, with stable hysteretic behavior exhibited up to 3.9% average axial strain and several specimens even reaching the desired core fatigue fracture. Nevertheless, the compressive

overstrength was large, which is indicative of a large friction coefficient, and several specimens failed with the timber restrainer splitting along the brace axis due to strong-axis bulging. A design method to prevent this failure mode was not provided. Yoshida et al. [10,11] conducted a series of cyclic tests of timber BRBs with the core plates sandwiched between two layers of glued laminated timber fixed with perpendicular timber boards and bolts. Several of the specimens achieved stable hysteresis loops up to 3.0% average axial strain. Haga et al. [12] investigated the effect of the bolt arrangement on the hysteretic properties of BRBs featuring core plates sandwiched between laminated timber pieces, which were bolted together with the glued interface oriented perpendicular to the core. Design methods were then developed for global buckling and bulging, but the predicted capacities disagreed with the experimental results.

These experiments indicate that timber restrainers are highly susceptible to bulging failures, where higher-mode buckling of the core plate induces a crushing or splitting failure in the timber restrainer. Although bulging is also a failure mode in BRBs with steel-mortar restrainers, it is easily prevented in these conventional BRBs using established design formula. Bulging also tends to occur in a ductile, confined punching shear mechanism that results in minimal loss of strength. In comparison, bulging of timber restrainers typically results in a rapid and complete loss of strength driven by crushing and splitting of the timber, a different mechanism that requires a new design method. This and other design criteria critical to the performance of BRBs [13,14] are not yet established for timber restrainers, including:

1. Restrainer and core tolerances designed to prevent global buckling
2. Restrainer designed to prevent local bulging failure
3. Connection and restrainer ends designed to prevent global instability including the connections
4. Cumulative deformation capacity until low-cycle fatigue failure of the core plates

The first three design criteria are limiting factors to the performance of MT-BRBs, degrading the hysteretic behavior and causing failure prior to achieving the full low-cycle fatigue capacity of the core plate.

The experimental program of this study included a range of scaled BRB specimens featuring mass timber restrainers with different reinforcing plates, bolted and glued connections, clearances and boundary conditions. These caused different types of failures in the timber restrainers, providing insight into the mechanism and ultimate capacity of each failure mode. The results were studied in detail and form the basis of newly proposed design methods, which proved successful in
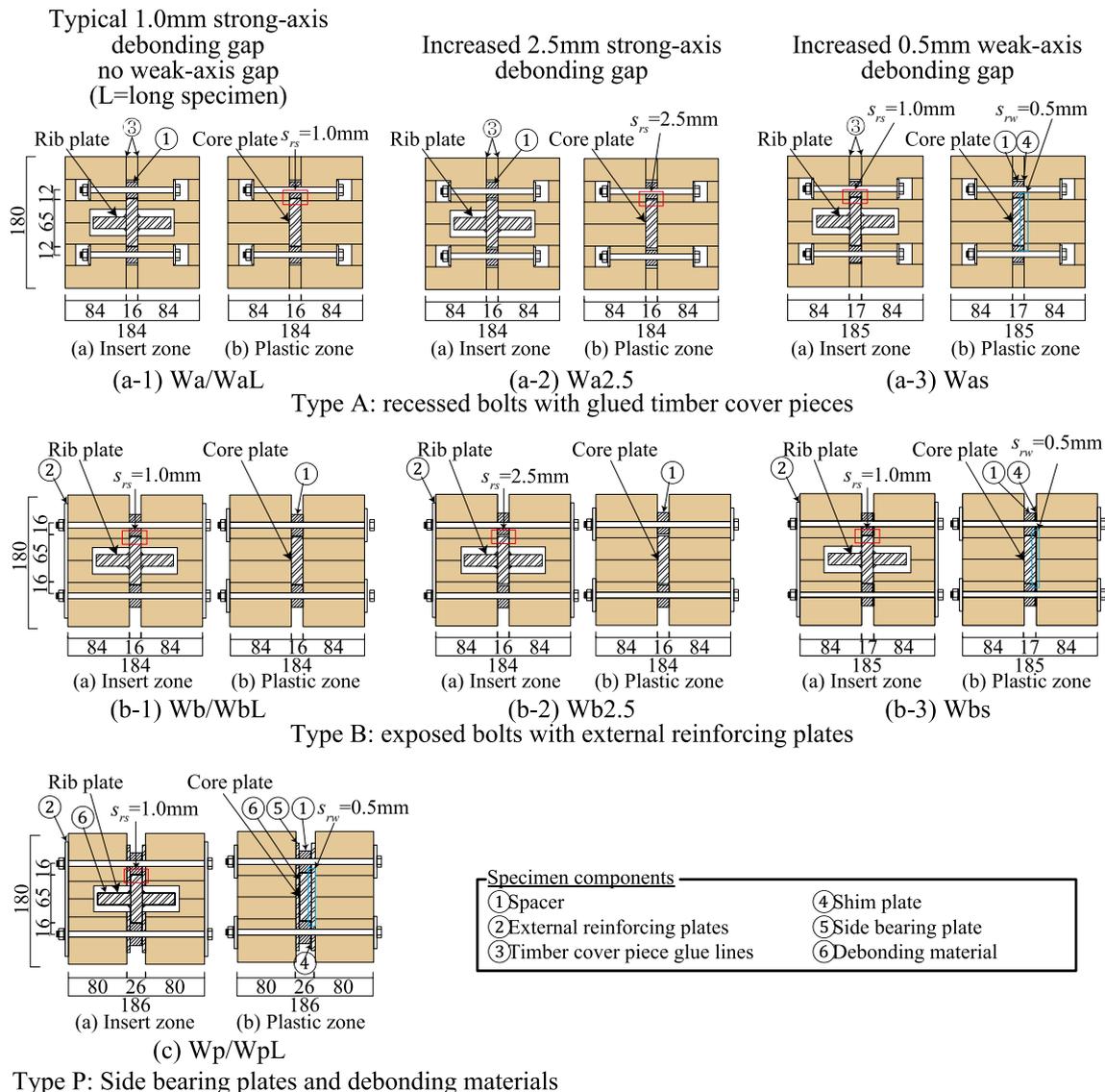

Fig. 1. Section summary of BRB specimens.

subsequent full-scale tests.

2. Cyclic loading tests of mass timber BRBs

2.1. Mass timber BRB specimens

Based on the observations of previous experiments, half-scale Mass Timber BRB (MT-BRB) specimens were designed to achieve a range of global buckling and bulging capacities, with the objective of inducing a range of failure modes in the timber restrainers. The cross-section of each test specimen is shown in Fig. 1, the restrainer assembly sequence in Fig. 2 and the specimen elevations in Fig. 3. Each test specimen employed a nominally identical 16 mm × 65 mm steel core plate (SN400B, yield stress 271 N/mm^2, ultimate tensile strength 427.3 N/mm^2) and a restrainer consisting of 2 pieces of 84 mm × 180 mm glue laminated timber (laminated larch E95-F315, Young's modulus 9,500 N/mm^2, bending strength 39.6 N/mm^2, cross-grain crushing strength at the center 9.7 N/mm^2 and edge 7.7 N/mm^2). The timber pieces were separated by steel spacers and connected with M8 bolts, with some specimens also featuring side bearing plates (Wp series), glued timber cover pieces or external reinforcing steel plates at the restrainer ends. Weak-axis buckling of the core plate was resisted by the glued laminated timber (and side bearing plates for the Wp series), while strong-axis buckling was resisted by the bolted steel spacers.

The Wa series featured recessed bolts and timber cover pieces glued across the gap formed by the steel spacers. The bolt recess had minimal effect, while the glued cover pieces slightly improved the response. Three clearances were investigated. The benchmark specimen (**Wa**) adopted a strong-axis debonding gap of $s_{rs} = 1.0$ mm (per face) between the core and spacers, but the core was placed directly against the timber to produce a weak axis debonding gap of $s_{rw} = 0$. This reduced the higher-mode buckling amplitude, thrust and bulging demands, but resulted in core binding during the compressive displacements and so necessarily relies on the flexibility of the soft timber to avoid excessive compressive forces. Two variations were then studied, including one specimen (**Wa2.5**) with a larger strong-axis debonding gap of $s_{rs} = 2.5$ mm, and a third (**Was**) with a small weak-axis debonding gap ($s_{rw} = 0.5$ mm) formed using thin shim plates.

The Wb series featured exposed bolts with exterior reinforcing plates at the restrainer ends, but lacked glued cover pieces. The external reinforcing plates enhanced the moment-transfer capacity at the restrainer end, which proved important for global stability of the long pinned specimens, but were unnecessary for the shorter bolted specimens with stiffened gussets. Similar to the Wa series, three variations were investigated. These included a benchmark specimen (**Wb**) with $s_{rs} = 1.0$ mm and no weak-axis debonding gap, a second specimen (**Wb2.5**) with an enlarged strong-axis debonding gap of $s_{rs} = 2.5$ mm, and a third

specimen (**Wbs**) with a small weak-axis debonding gap of $s_{rw} = 0.5$ mm.

The Wp series was similar to the Wb series, but added 4.5 mm thick bearing plates on both sides of the core (held in place by the bolts and friction) to help distribute the outward force imposed by the core weak-axis higher-mode buckling. Just one short specimen (**Wp**) was tested, featuring the standard strong-axis debonding gap of $s_{rs} = 1.0$ mm and a small weak-axis debonding gap of $s_{rw} = 0.5$ mm.

The final L series (**WaL**, **WbL** and **WpL**) featured pinned connections and longer 3.55 m pin-to-pin lengths, but these were otherwise identical to the shorter benchmark specimens (Wa, Wb, Wp). These specimens investigated the moment-transfer mechanism and global stability. The timber restrainers were designed using the global stability method described later in Equations (26) to (27), and featured bolts spaced at 100 mm, but with a smaller pitch at the restrainer ends. Also, stiffeners were welded to the ends of the rectangular steel cores to form a cruciform shape along the elastic zone and prevent local buckling. A total of 10 short and long specimens were fabricated for this test. The restrainer assembly process is outlined in Fig. 2. One glued laminated timber piece was laid facing upwards, the core plate and second glued laminated timber piece placed on top and the bolts inserted. The specimen was then turned 90° to fasten the nuts. The assembly of the Wp series specimens only differed by stacking additional side bearing plates and attaching external reinforcing plates at the restrainer end, as depicted in steps (4) and (5) of Fig. 2.

2.2. Test program

Each MT-BRB specimen was tested at Tokyo Institute of Technology using the test frame depicted in Fig. 4. Cyclic loading was applied to the sliding table using an actuator with a maximum horizontal force of 500kN and maximum amplitude of about ± 200 mm. Both the short and long specimens were fixed to the reaction frame at the top and sliding table at the bottom, with inclined angles of $\theta = 39°$ and $\theta = 25°$, respectively. The quasi-static loading protocol shown in Fig. 5 was applied, consisting of three cycles each at ± 0.1%, 0.5%, 1.0%, 2.0% and 3.0% average axial strain, which is defined as the axial displacement (excluding the connection displacement) divided by the core plastic length. After the third cycle at ± 3.0%, constant amplitude cycles at 3.0% were continued until the core fractured or the timber restrainer failed.

The instrumentation is shown in Fig. 6. The horizontal actuator force, axial displacement, relative axial and transverse displacements of two timber restrainer pieces and strains at the external reinforcing plates were directly measured. LVDTs were used to record the displacements, with the relative restrainer measurements obtained by attaching a target on the opposite timber piece. The BRB axial force (*N*) was calculated from the actuator force and inclined angle, while the average axial stress
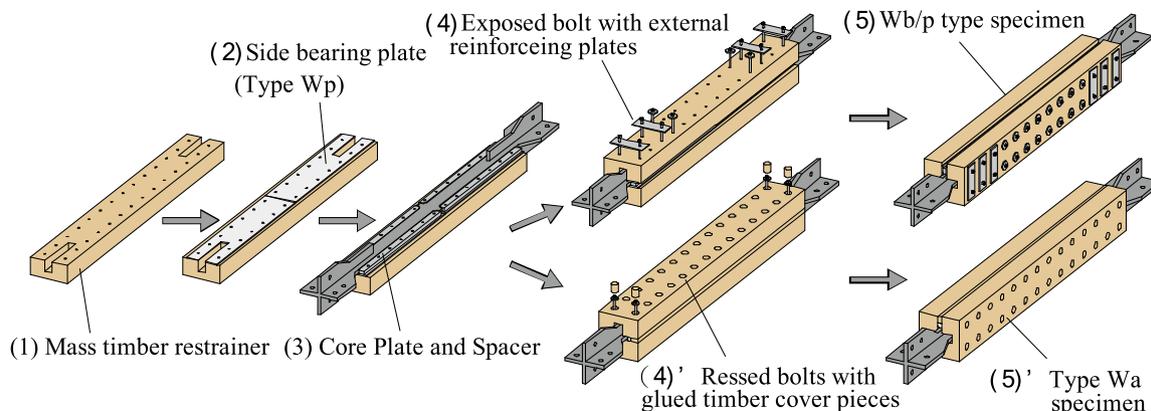

(2) Side bearing plate (Type Wp)

(4) Exposed bolt with external reinforceing plates

(5) Wb/p type specimen

(1) Mass timber restrainer   (3) Core Plate and Spacer

(4)' Ressed bolts with glued timber cover pieces

(5)' Type Wa specimen

Fig. 2. Assembly of BRB with mass timber restrainer.

(a) Short BRB specimens

(b) Long BRB specimens
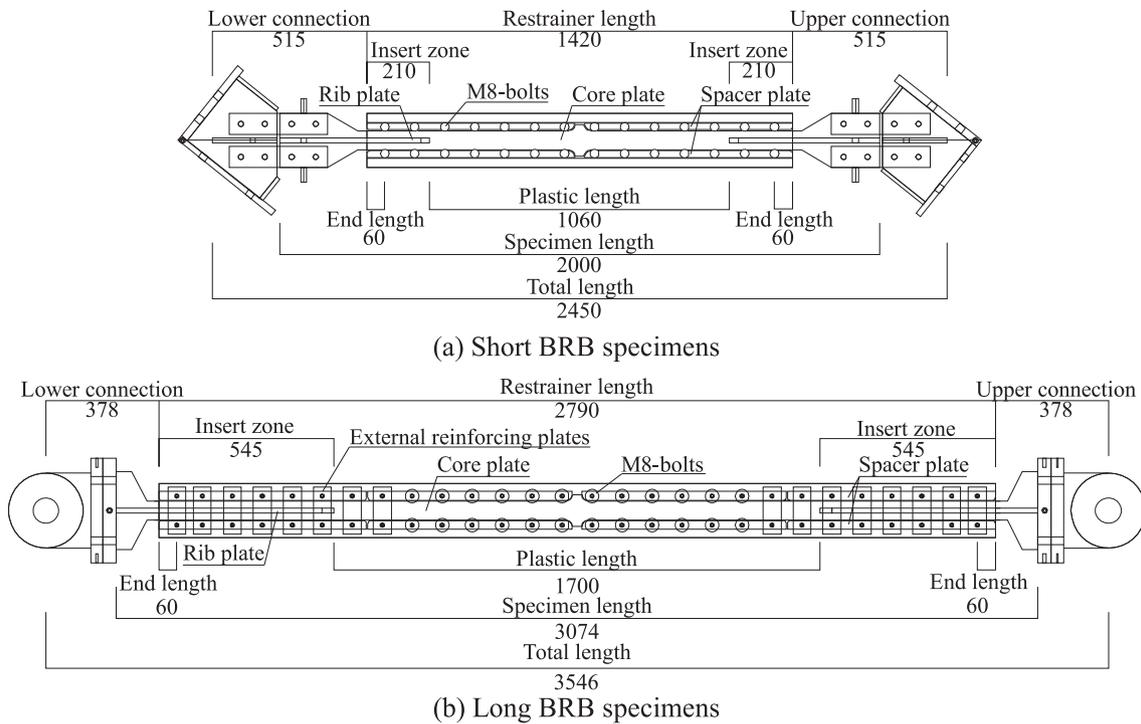
Fig. 3. Elevation summary of BRB specimens.

(a) Long BRB   (b) Short BRB
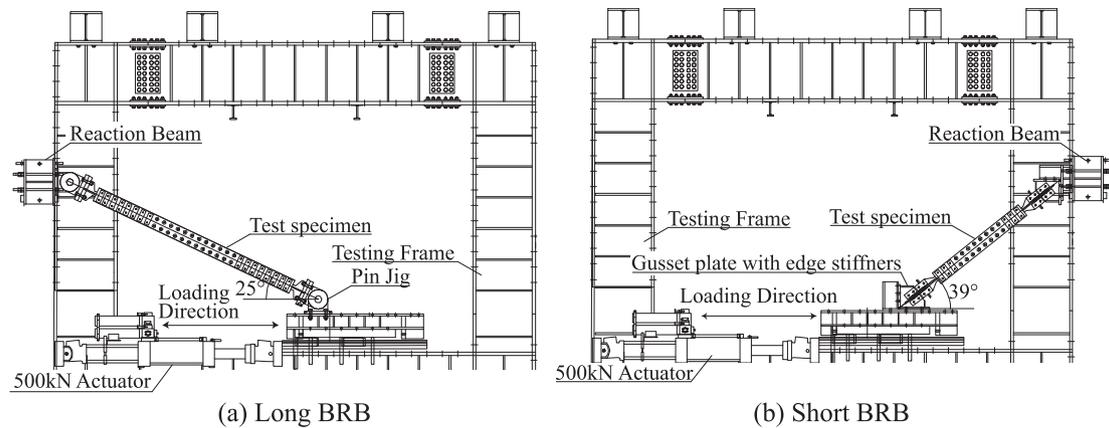
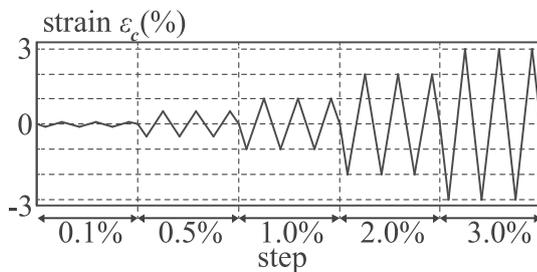**Fig. 4.** Test set-up.

Fig. 5. Loading protocol.

σ_c was calculated as N/A_c, where A_c is the initial core yield area (1040 mm^2). The average axial strain ε_c was estimated as δ/L_p, where δ is the measured axial deformation excluding the connections (⑤ in Fig. 6) and L_p the initial core plastic length (1060 mm or 1700 mm). Strains at the external reinforcing steel plates were measured using strain gauges and used to check for incipient signs of global instability.

2.3. Test results of long BRBs

The long MT-BRB specimens (L series) provided insight into the restrainer-end moment-transfer mechanism and global stability of BRBs with timber restrainers. The average axial stress–strain relationships are shown in Fig. 7 and the failure modes in Fig. 8. Table 1 details the first cycle with timber restrainer cracking, the final step at failure, the maximum compression-to-tension force ratio (β_{max}), the cumulative strain energy normalized by the core yield stress and the failure mode of each specimen.

(a) WaL: 0.5%-1st cycle, Timber rupture → Global buckling, Fig. 7 (a), Fig. 8(a), (b)

The long WaL specimen (Wa series) immediately rotated at the lower pinned connection as compression force was applied (1st cycle at 0.5%
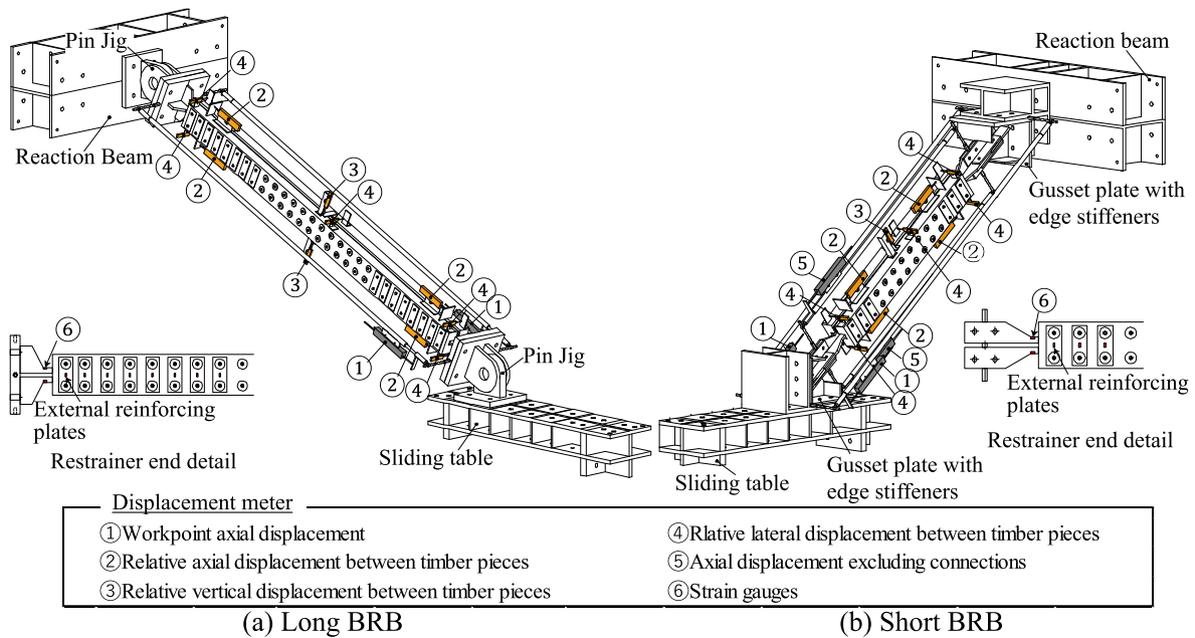
Fig. 6. Instrumentation plan.

Displacement meter
① Workpoint axial displacement
② Relative axial displacement between timber pieces
③ Relative vertical displacement between timber pieces
④ Rlative lateral displacement between timber pieces
⑤ Axial displacement excluding connections
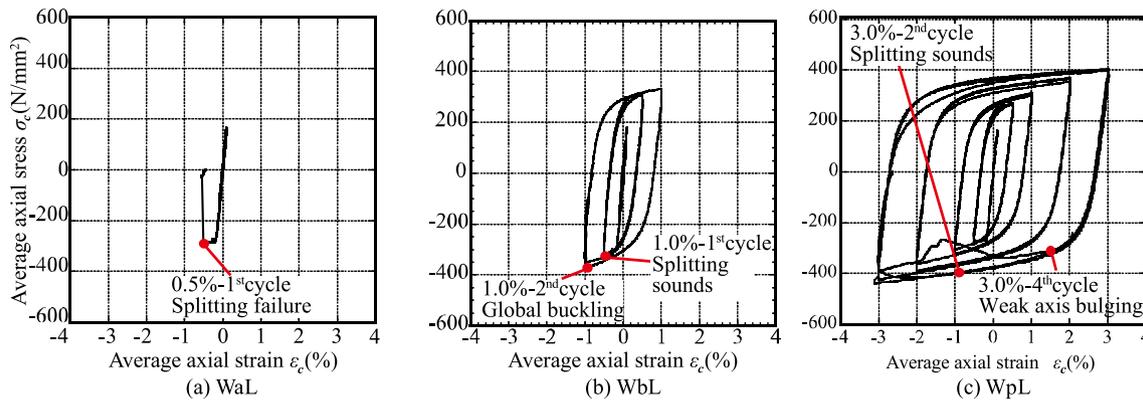⑥ Strain gauges

(a) Long BRB   (b) Short BRB

Fig. 7. Average stress–strain relationships of Long MT-BRBs.

strain). The transfer moment split the end of the timber restrainer, and without reinforcing steel plates to curtail the splitting this led to a brittle global buckling failure mode.

(b) WbL: 1.0%-2nd cycle, Global instability including connection, Fig. 7(b), Fig. 8(c)

The long WbL specimen (Wb series) featured external reinforcing plates connecting the bolts at the restrainer ends, which provided a backup moment transfer mechanism. However, cracking was heard as the core plate rotated and bore against the restrainer during the third compression cycle (1.0%-1st cycle), and cracks were observed at the end of the timber restrainer between the vertical reinforcing plates. While the external reinforcing plates prevented uncontrolled crack growth, the cracks still increased the P-Delta demands at the restrainer end during the next compression cycle (1.0%-2nd cycle). This caused the core plate to yield just outside of the restrainer and precipitated global instability with a plastic hinge at the neck.

(c) WpL: 3.0%-4th cycle, Local weak-axis bulging rupture, Fig. 7(c), Fig. 8(d)

Finally, the long WpL specimen (Wp series) was reinforced with bearing plates placed on both sides of the core and cut into top and bottom parts near the restrainer ends to accommodate the core stiffeners (see step (2) in Fig. 2). WpL exhibited stable hysteresis loops through the full ascending protocol. The timber restrainer cracked during the fatigue protocol (3.0%-4th cycle), causing a drop in the compression force before recovering a substantial residual capacity (Fig. 8(d)). The post-test specimen deconstruction confirmed that higher-mode buckling of the core plate caused a bulging failure, with the weak-axis force from the core plate pushing out and plastically deforming the side bearing plates. Nevertheless, the longitudinal continuity of these side plates at the restrainer end provided effective moment-transfer capacity between the core and timber restrainer, preventing global buckling and improving the overall performance.

It is notable that the connection length ratios ($\xi = 0.11$ in Fig. 19) of WaL, WbL and WpL were about 50% longer than the pinned MT-BRBs tested by Murphy et al. [13], which were stable despite lacking reinforcing plates. The longer connections increased the buckling and moment-transfer demands in this test, exposing the limited moment-transfer capacity of unreinforced timber restrainers.
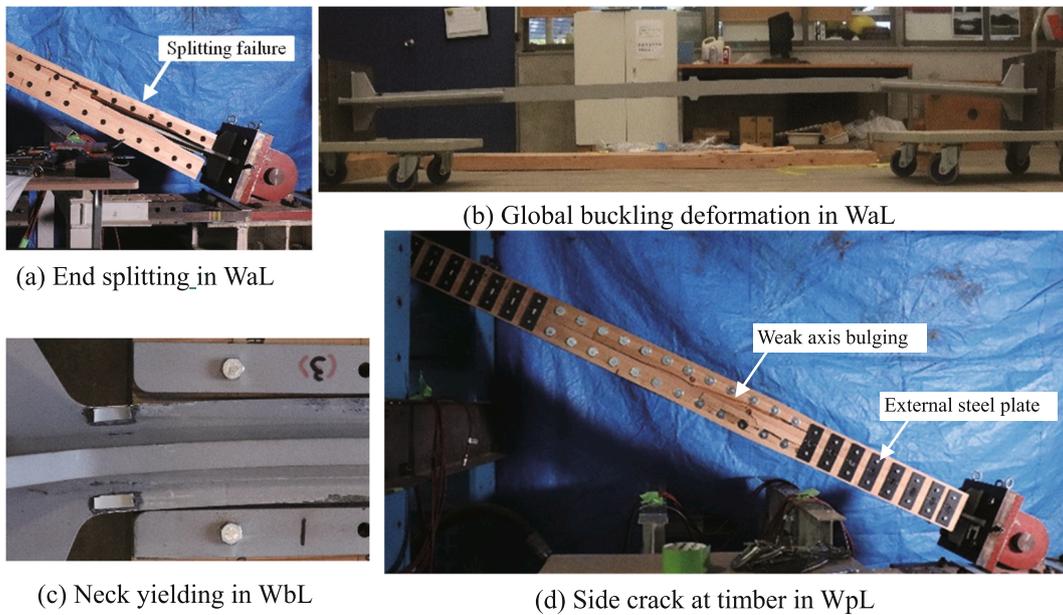
(a) End splitting in WaL

(b) Global buckling deformation in WaL

(c) Neck yielding in WbL

(d) Side crack at timber in WpL

Fig. 8. Failure modes of Long MT-BRBs.

Table 1
Summary of test results.

Name	Splitting Step	Fractured Step	β_{max}	Cumulative strain	Failure Mode
WaL	0.5%-1cycle	0.5%-1cycle	1.01	0.5%	Global buckling (restrainer end splitting)
WbL	1%-1cycle	1%-1cycle	1.07	8.9%	Global buckling (neck yielding)
WpL	3%-2cycle	3%-4cycle	1.08	76.3%	Weak-axis bulging (splitting)
Wa	2%-1cycle	3%-6cycle	1.12	111.9%	Strong-axis bulging (splitting)
Wb	2%-1cycle	3%-4cycle	1.09	82.3%	Strong-axis bulging (splitting)
Wa2.5	2%-1cycle	3%-4cycle	1.32	80.8%	Strong-axis bulging (splitting)
Wb2.5	2%-2cycle	3%-3cycle	1.07	66.3%	Strong-axis bulging (splitting)
Was	2%-2cycle	3%-1cycle	1.11	35.8%	Weak-axis bulging (splitting)
Wbs	2%-2cycle	3%-1cycle	1.06	36.0%	Weak-axis bulging (splitting)
Wp	3%-2cycle	3%-4cycle	1.11	76.9%	Weak-axis bulging (splitting)

2.4. Test results of short BRBs

The short MT-BRB test specimens (Wa, Wb and Wp series) provided insight into the bulging failure modes. The average axial stress–strain relationships are shown in Fig. 9 and the failure modes in Fig. 10, with key results summarized in Table 1.

(d) Wa: 3.0%-6th cycle, Strong-axis local bulging failure + timber rupture, Fig. 9(a), Fig. 10(a)

The benchmark Wa specimen (Wa series) featured recessed bolts and glued timber cover pieces, and successfully achieved a stable hysteresis through the 6th cycle at 3.0% strain (Fig. 9(a)). However, the compressive force gradually increased through the 3.0% cycles as higher-mode buckling caused the plate to dig into the timber restrainer, producing $\beta = 1.12$. The specimen eventually failed after a cumulative strain of 112% in strong-axis bulging, which resulted in a complete loss of strength.

(e) Wb: 3.0%-4th cycle, Strong-axis local bulging failure + timber rupture, Fig. 9(b)

The benchmark Wb specimen (Wb series) featured an exposed bolted restrainer. The compressive force gradually increased through the 2.0% cycles and the specimen failed with strong-axis bulging in the 4th cycle at 3.0% strain, which was slightly earlier than Wa. The outward bulging force applied bending demands to the bolts, splitting the timber restrainer and resulting in a rapid, but not total loss of strength.

(f) Wa2.5: 3.0%-4th cycle, Strong-axis local bulging failure + timber rupture, Fig. 9(d), 10(a)

The Wa2.5 specimen (Wa-series) featured an enlarged strong-axis debonding gap of s_{rs} = 2.5 mm per face, which more than doubled the strong-axis bulging force demand applied to the spacers and bolts. This caused strong-axis bulging coinciding with a bolt row during the 4th cycle at 3.0% strain (Fig. 10(a)), which was slightly earlier than the strong-axis bulging failure of the benchmark Wa specimen. As noted in Table 1, the performance of Wa2.5 exceeded Wb2.5 by one cycle, suggesting that the glued timber cover pieces marginally enhanced the strong axis bulging resistance.

(g) Wb2.5: 3.0%-3rd cycle, Strong-axis local bulging failure + timber rupture, Fig. 9(e), 10(c)

The Wb2.5 specimen (Wb-series) featured an enlarged 2.5 mm strong-axis debonding gap. This specimen failed due to strong-axis bulging during the 3rd cycle at 3.0% strain, which was one cycle less than Wa2.5.
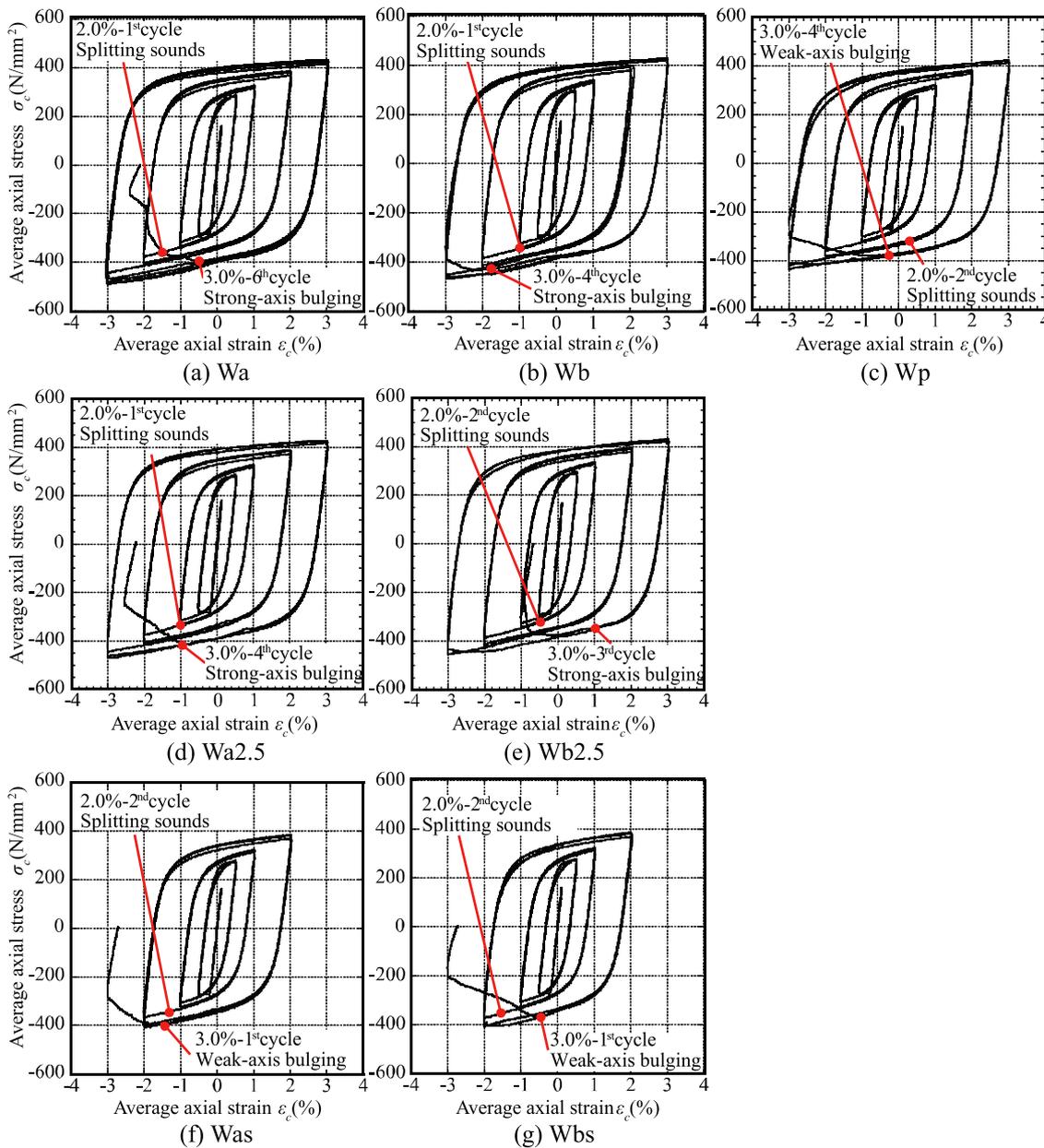
Fig. 9. Average stress–strain relationships of Short MT-BRBs.

(h) Was: 3.0%-1st cycle, Weak-axis local bulging failure + timber rupture, Fig. 9(f), 10(b)

The Was specimen (Wa series) featured a weak-axis debonding gap of $s_{rw} = 0.5$ mm per face and failed due to weak-axis buckling with the core crushing the timber during the 1st cycle at 3.0% strain (Fig. 10(b)). This was a substantial reduction in performance compared to the 6 cycles at 3.0% achieved by the benchmark Wa specimen, which lacked a weak-axis gap. However, the performance was identical to Wbs, suggesting that the glued timber cover piece had a negligible effect on the weak-axis bulging resistance.

(i) Wbs: 3.0%-1st cycle, Weak-axis local bulging failure + timber rupture, Fig. 9(g), 10(d)

The Wbs specimen (Wb series) featured a 0.5 mm weak-axis debonding gap per face and failed in weak-axis bulging with the core plate crushing and cracking the timber restrainer during the 1st cycle at

3.0% strain (Fig. 10(d)). This performance was identical to the Was specimen.

(j) Wp: 3.0%-4th cycle, Weak-axis bulging failure, Fig. 9(c), Fig. 10 (e)-(g)

The benchmark Wp specimen (Wp-series) featured side bearing plates and achieved stable hysteresis loops until failing in the 4th cycle at 3.0% strain (Fig. 9(c)). Compared to the Was and Wbs specimens, which featured the same 0.5 mm small weak-axis debonding gap, the Wp specimen achieved three more cycles at 3.0% before bulging, suggesting that the side bearing plates were effective in delaying weak-axis bulging. This performance was identical to the longer WpL specimen, which also failed due to weak-axis bulging in the 4th cycle at 3.0% strain, suggesting that the yield length has negligible influence on bulging failure modes. Although this specimen failed in bulging, which is undesirable, this occurred about the core weak-axis and the failure was far more ductile than the Wa and Wb bulging failures, retaining significant
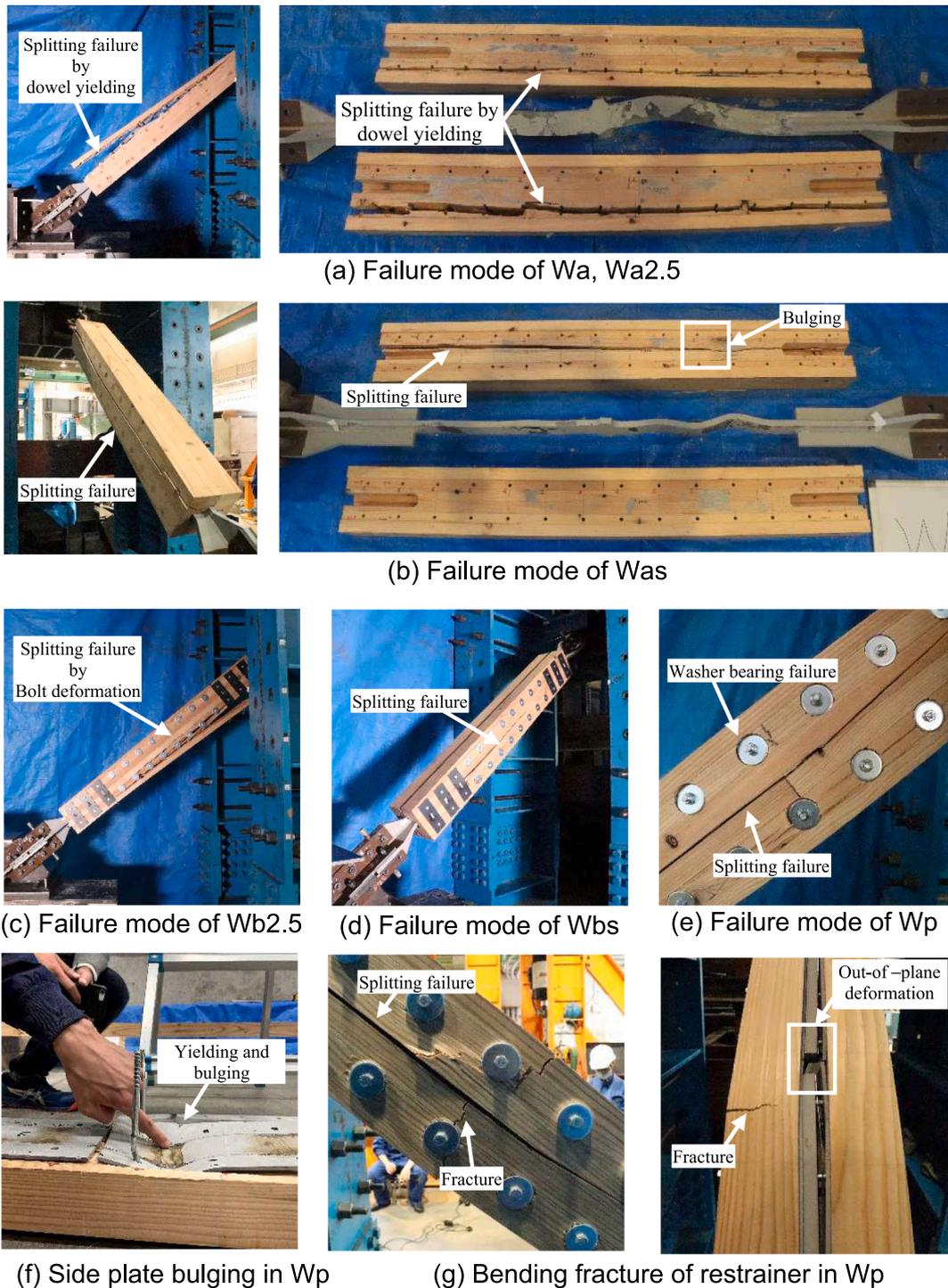
(a) Failure mode of Wa, Wa2.5

(b) Failure mode of Was

(c) Failure mode of Wb2.5 (d) Failure mode of Wbs (e) Failure mode of Wp

(f) Side plate bulging in Wp (g) Bending fracture of restrainer in Wp

Fig. 10. Failure modes of Short MT-BRBs.

residual strength. Bulging caused the timber restrainer to split (Fig. 10 (e)-(g)), and the post-test deconstruction (Fig. 10(f)) observed substantial plastic deformation of the side bearing plates, which helped distribute the outward bulging force to the four adjacent bolts.

2.5. Discussion on the configuration and performance of MT-BRBs

1) Restrainer end reinforcement and moment-transfer capacity

As indicated by the long test specimen results in Section 2.3 (a)-(c), the restrainer-end moment-transfer capacity of MT-BRBs was much lower than conventional BRBs. This was true despite the long core elastic segment insert lengths (L_{in} / B_n = 545 / 65 = 8.3, where B_n is the width of the neck, or ribbed core section immediately outside the restrainer and L_{in} is length that this enlarged section is inserted into the restrainer), which far exceeded the recommended insert ratios (L_{in} / B_n > 2) that have previously been found to provide full flexural continuity in mortar-filled steel tube BRBs [15]. The restrainer-end moment-transfer capacity was enhanced when continuous steel plates were bolted in the longitudinal direction at the restrainer end (as for WpL), but was only minimally improved by adding external vertical reinforcing plates (WbL).

2) Boundary conditions and global stability

Significant restrainer-end moment-transfer capacity was only achieved when steel plates reinforced the ends of the timber restrainer. Nevertheless, the low moment-transfer capacity of MT-BRBs increases the risk of global buckling, particularly for longer pinned connections. This may be addressed by adopting the "cantilevered connection" stability concept [13,15] with stiff boundary conditions, such as bolted connections with stiffened gusset plates.

3) Timber restrainer bolted/glued connections and bulging

No noticeable difference was observed when recessing the bolts (Wa series) compared to externally fixing the bolts and washers (Wb series). Conversely, while the glued timber cover pieces (Wa series) had no effect on weak-axis bulging, these did slightly enhance the resistance to strong-axis bulging.

4) Core debonding gaps and bulging

The strong and weak-axis debonding gaps, or lack thereof, significantly influenced the outwards bulging demands, with larger gaps causing bulging to occur earlier. Timber restrainers are unique in that the weak-axis gap is often omitted to reduce the core thrust, but this causes core binding. While not acceptable in conventional BRBs with strong and stiff confinement, weak-axis core binding may be a reasonable tradeoff in MT-BRBs, as the timber offers minimal confinement and these tend to be governed by bulging.

Nevertheless, the sensitivity of bulging to the debonding gap thickness suggests that the gaps must be tightly controlled, particularly in the weak-axis direction, as increasing the gap from zero (Wa) to $s_{rw} = 0.5$ mm (Was) caused bulging to occur two cycles earlier (5 vs 3 cycles at 3.0% strain) for the Wa series. However, the debonding gaps of the Wa and Wb series may be affected by timber dimensional stability with changes in ambient humidity, and so a degree of conservatism is warranted.

5) Reinforcing side bearing plates and weak-axis bulging

The side bearing plates placed on both sides of the Wp specimen cores improved the resistance to weak-axis bulging and ductility of this failure mode. However, the primary function of these plates was to distribute the outwards bulging force to the adjacent bolts and so their effectiveness may vary depending on the bolt pitch and plate thickness. Nevertheless, while stiff bearing plates may delay bulging, they are unlikely to completely eliminate weak-axis bulging, which remains a critical failure mode for MT-BRBs.

3. Design methods for MT-BRBs

A wide range of global buckling and local bulging failure modes were observed throughout the MT-BRB test program. The causative

mechanism was investigated for each failure mode and design equations developed to accurately capture the pertinent demands and capacities.

3.1. Failure mode mechanisms

a) Strong-axis local bulging failure

Failure mechanisms leading to strong-axis bulging for each specimen type are depicted schematically in Fig. 11. Timber crushing against the bolts (Fig. 11(a) and (b)) was observed for the Wa, Wb, Wa2.5 and Wb2.5 specimens. Strong-axis higher-mode buckling pushes the core plate against the steel spacers, which deform the bolts as they are pushed against the timber. The bulging resistance is then ultimately governed by the timber bearing strength. Conversely, bolt yielding (Fig. 11(c)) was observed for the Wp and WpL specimens. The self-reacting side bearing plates resist the opposing thrust of alternating strong-axis higher-mode buckling wavecrests and load the bolts. This causes the bolts to act like short dowels and ultimately fail in shear without loading the timber.

b) Weak-axis local bulging failure

Failure mechanisms leading to weak-axis bulging for each specimen type are depicted schematically in Fig. 12. Timber crushing or splitting (Fig. 12(a) and (b)) was observed for the Was, Wbs, Wp and WpL specimens. Weak-axis higher-mode buckling pushes the core plate directly against the timber, either crushing the timber at a core wavecrest, splitting the timber in bending, or crushing the timber at the bolt washers. Timber crushing and splitting (Fig. 12(c)) were also observed for the Wp series specimens, but these were preceded by yielding of the side bearing plates, which helped distribute the outward force of the core plate, but more importantly provided ductility and enhanced the residual post-bulging strength.

c) Global buckling including connections

The long WaL and WbL specimens failed in global buckling due to insufficient moment-transfer capacity. Bending moments are transferred from the core to restrainer by lever action along the core insert lengths (Fig. 13), but are limited by crushing and splitting of the timber, which occurred at the end-most bolt row in this test. WaL failed prior to achieving the plastic axial-flexural capacity of the "neck" (core section immediately outside the restrainer), while timber splitting in WbL caused the restrainer end to rotate before the external reinforcing plates could be engaged, delaying buckling by just one cycle. Given these low restrainer-end moment-transfer capacities, it may be necessary to cantilever the connections off the gusset to maintain global stability [13,15].

3.2. Design criteria proposal for timber restrainers
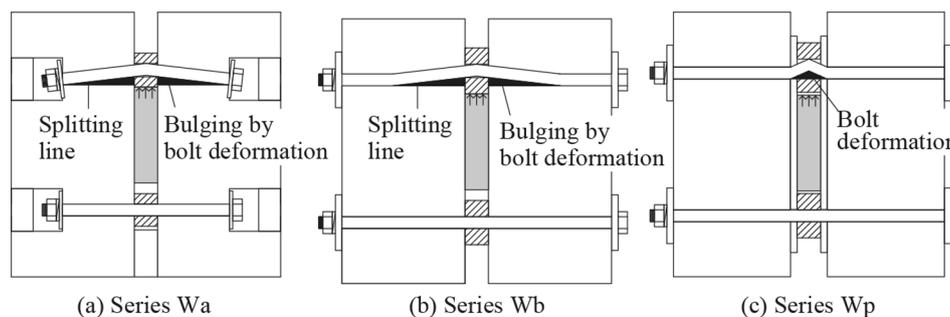
1) Strong- and weak-axis bulging demand

(a) Series Wa   (b) Series Wb   (c) Series Wp

Fig. 11. Strong-axis bulging failure mechanisms.

Fig. 12. Weak-axis bulging failure mechanisms.

(a) Series Wa   (b) Series Wb   (c) Series Wp
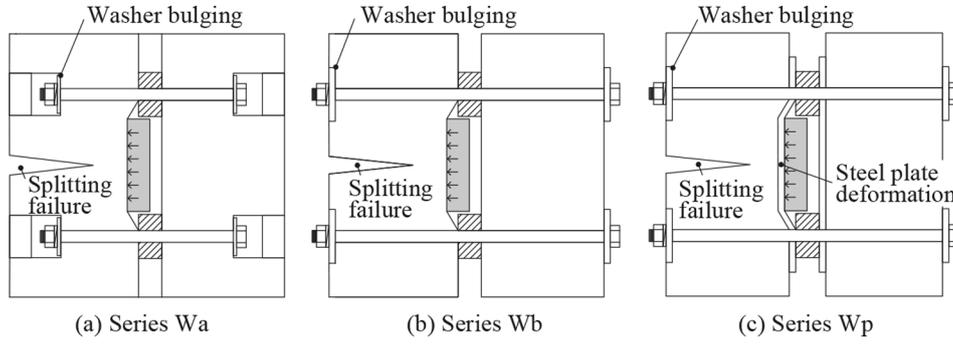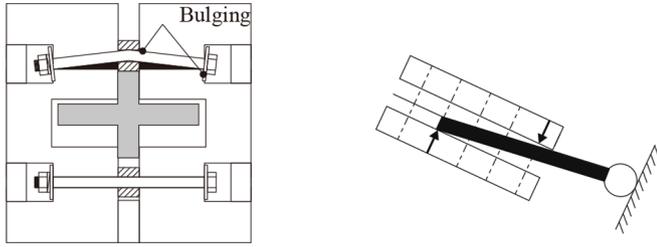

Fig. 13. Restrainer-end moment-transfer failure mechanism.

The outward bulging forces ($P_{d,s}$, $P_{d,w}$) (Fig. 14) applied at the core plate higher-mode buckling wavecrests may be estimated by Equations (1) and (2) [13,16,17]. Note that the weak-axis amplitude includes a second-order restrainer stiffness term (K_r) [18], which is given by Equations (3)–(6).

$$P_{d,s} = \frac{4N_{cu}(2s_{rs} + \nu_p B_c \varepsilon_t)}{l_{ps}}, \quad (strong-axis)$$

$$P_{d,w} = \frac{4N_{cu}(2s_{rw} + \nu_p t_c \varepsilon_t)}{l_{pw} - 4N_{cu}/K_r}, \quad (weak-axis)$$
(1-2)

$$K_r = \frac{1}{1/K_w/1/K_b}, \quad K_b = \frac{E_b A_{eff}}{D_r/2}, \quad K_w = \frac{E_w l_{pw} B_r}{D_{rh}}$$
(3-5)

$$A_{eff} = 2 \times \frac{\pi d^2}{4} \cdot \frac{l_{pw}}{l_b}$$
(6)

Where, N_{cu}: maximum core compression force, s_{rs}, s_{rw} strong and weak-axis gaps (per face), l_{ps}, l_{pw}: strong and weak-axis wavelengths, estimated as $l_{ps} = 6B_c$ and $l_{pw} = 9t_c$ from Ref. [13] and test observations,
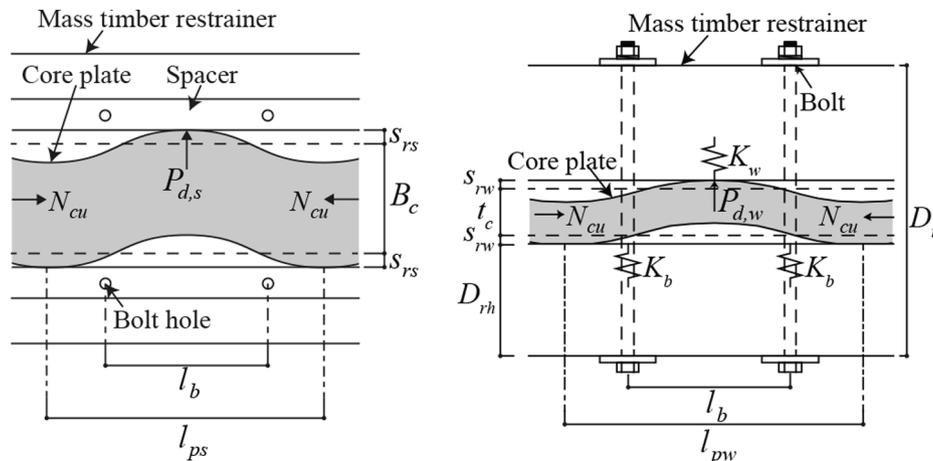
ν_p: plastic Poisson ratio (=0.5), t_c, B_c: core plate thickness and width, ε_t: tensile strain, K_r: restrainer stiffness, D_r: restrainer width, d: bolt diameter, E_w: timber elastic modulus, E_b: bolt elastic modulus.

2) Strong-axis bulging capacity: bolt deformation and timber splitting

Strong-axis bulging caused by timber splitting (Fig. 15) is a function of the bolt contact width and stress concentration. These vary with the bolt and timber dimensions, but may be estimated using an equivalent width D_r / α following [19,20]. The capacity for this splitting failure is then given by Equations (7), (8).

$$P_{c,s1} = \alpha_{spl} \cdot F_{wu} \cdot d \cdot \frac{D_r}{\alpha},$$

$$\alpha = \frac{1}{0.46 + 11.6 E_b d^3 / k \cdot D_r^4}$$
(7-8)

Where, F_{wu}: bearing strength of timber, α_{spl}: margin between bolt impact and timber splitting (taken as $\alpha_{spl} = 2.5$ based on the test results), α: equivalent timber width of the bolt in bending, and k (N/mm³): unit timber stiffness [19,20].
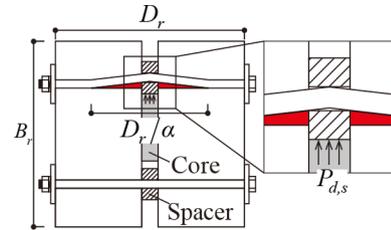

Fig. 15. Splitting failure due to bolt deformation.

Fig. 14. Outward force due to local buckling [13].

3) Strong-axis bulging capacity: bolt shear

Strong-axis bulging may be limited by bolt shear as the core bulging force is transmitted to the timber through the spacers and bolts. The capacity for bolt shear fracture is given by Equation (9).

$$P_{c,s2} = 2 \times \frac{\pi d^2}{4} \times \frac{\sigma_{bu}}{\sqrt{3}} \times \frac{B_c}{l_b} \quad (9)$$

Where, B_c: core plate width, which in this equation represents the width over which the bulging force is distributed, l_b: bolt spacing, σ_{bu}: bolt ultimate tensile strength.

4) Weak-axis bulging capacity: timber bearing at core wavecrest

The outward force at the weak-axis higher-mode buckling wave-crests tends to be concentrate over an area of approximately $t_c \times B_c$ [17], such that the timber bearing capacity may be estimated from Equation (10).

$$P_{c,w1} = t_c \times B_c \times F_{wu} \quad (10)$$

5) Weak-axis bulging capacity: timber bearing at bolt washer

The number of bolts resisting the outward force of a single wavecrest may be estimated assuming a 30-degree spread angle (Fig. 16, with $t_p = 0$). The washer bearing capacity is then given by Equation (11), (12).

$$P_{c,w2} = 2A_w \times \frac{(2D_{rh}/\sqrt{3} + t_c)}{l_b} \times F_{wu}$$
$$A_w = \frac{\pi(D_{wo}^2 - D_{wi}^2)}{4} \quad (11, 12)$$

Where, D_{rh}: width of each timber half, D_{wo}, D_{wi}: washer inner and outer diameters, A_w: washer area.

6) Weak-axis bulging capacity: timber bending

Bolts hold the timber restrainer together and act as discrete supports resisting the outward bulging force, producing a bending moment in the timber between the bolts (Fig. 16). The capacity is given by Equation (13) for the uniform force distribution and bending moment diagram shown in Fig. 17 (with $t_p = 0$).

$$P_{c,w3} = \frac{4 \times (t_c + 2 \times D_{rh}/3\sqrt{3}) \times D_{rh}^2}{3(B_c + 4b)} F_{wbT} \quad (13)$$

Where, b: distance from the core edge to bolt line, F_{wbT}: timber bending strength perpendicular to the grain, assumed to be 10% of bending strength parallel to the grain.

7) Strong-axis bulging capacity (with side bearing plates): timber bearing at bolt
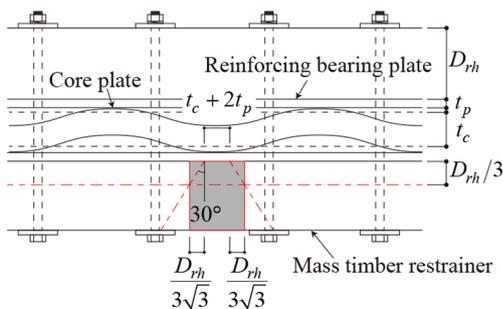

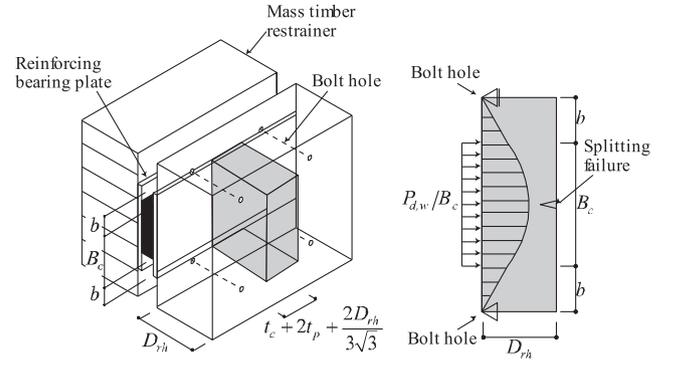Fig. 16. Distribution assumption for outward force along weak axis.

Fig. 17. Bending moment assumption for timber restrainer side.

When side bearing plates are provided (Wp series), the strong-axis bulging force is resisted through internal reactions within the steel plates and so the timber bearing strength need not be checked. Instead, the steel bearing strength at the bolt holes is determined by Equation (14).

$$P_{c,s2-p} = 2t_p d \times \frac{B_c}{l_b} \times \sigma_{pu} \quad (14)$$

Where, t_p: side bearing plate thickness, σ_{pu}: side bearing plate ultimate strength.

8) Strong-axis bulging capacity (with side bearing plates): bolt shear

The bolt shear capacity is the same as Equation (9), even with side bearing plates (Wp series).

$$P_{c,s2} = 2 \times \frac{\pi d^2}{4} \times \frac{\sigma_{bu}}{\sqrt{3}} \times \frac{B_c}{l_b} \quad (15)$$

9) Weak-axis bulging capacity (with side bearing plate): timber bearing at core wavecrest

Side bearing plates help distribute the bulging force, and so the bearing capacity at the core wavecrests is increased from Equation (10) to include a 45-degree spread angle through the steel plates.

$$P_{c,w1-p} = (t_c + 2t_p) \times (B_c + 2t_p) \times F_{wu} \quad (16)$$

10) Weak-axis bulging capacity (with side bearing plates): timber bearing at bolt washer

Distributing the bulging force through the side bearing plates, Equation (11) is modified to Equation (17).

$$P_{c,w2-p} = 2A_w \times \frac{(2D_{rh}/\sqrt{3} + t_c + 2t_p)}{l_b} \times F_{wu} \quad (17)$$

11) Weak-axis bulging capacity (with side plates): timber bending

Distributing the bulging force through the side bearing plates, Equation (13) is modified to Equation (18) (Fig. 17).

$$P_{c,w3-p} = \frac{4(t_c + 2t_p + 2D_{rh}/3\sqrt{3})D_{rh}^2}{3(B_c + 4b)} F_{wbT} \quad (18)$$

12) Weak-axis bulging capacity (with side bearing plates): side plate bearing

Side bearing plates were found to provide substantial ductility to the

bulging failures of Wp and WpL, preventing a complete loss of strength. To ensure that the plate is effective, a plastic yield line analysis (Fig. 18) [13] may be evaluated using a 5-yield line model that is valid for $B_c > 0.7\,B_b$.

$$P_{c,w4-p} = \frac{2t_p^2 \cdot \sigma_{py}}{\sqrt{1 - B_c/B_b}} \qquad (19)$$

Where, σ_{py}: side bearing plate yield strength, B_b: transverse bolt spacing (in core width direction).

13) Global stability limit including connection

The global buckling capacity of MT-BTBs is likely to be limited by the restrainer-end moment transfer capacity due to the same reasons that bulging often governs. This stability limit is sensitive to the connection and boundary conditions, and may be evaluated from Equations (20)–(25) following [13,15].

$$N_{\lim 1} = \frac{\left(M_p^r - M_0^r\right)\Big/a_r + N_{cr}^r}{\left(M_p^r - M_0^r\right)\Big/\left(a_r N_{cr}^B\right) + 1} > N_{cu}^{ep} \qquad (20)$$

$$M_p^r = \min\left(M_p^{r-rest}, M_p^{r-neck}\right) \qquad (21)$$

$$M_p^{r-neck} = \left\{1 - \left(\frac{N_{cu} - N_{wy}^c}{N_u^c - N_{wy}^c}\right)^2\right\} Z_p \sigma_{py} \qquad (22)$$

$$M_p^{r-rest} = P_{c,s1} \times (L_{in} - l_{be}) \; or \; M_p^{r-rest} = Z_t \sigma_{tb} \qquad (23\text{-}24)$$

$$a_r = e + s_{rs} + \xi L_0\left(\theta_0 + \frac{2s_{rs}}{L_{in}}\right) \qquad (25)$$

Where, M_p^{r-rest}: restrainer-end moment-transfer capacity, M_p^{r-neck}: plastic moment capacity of the core neck, reduced for the axial load, M_p^r: restrainer-end plastic moment capacity, M_0^r: initial bending moment, ξL_0: connection length, L_{in}: insert length, l_{be}: end distance to first bolt row, N_{cr}^B: elastic buckling load, N_{cr}^r: elastic buckling load of cantilevered connection, N_{cu}: axial yield force of cruciform neck, N_{wy}^c: axial yield force of neck "web" (vertical plate), a_r: initial imperfection at neck, e: force eccentricity, θ_0: initial rotation angle at restrainer end, Z_t: timber section modulus, σ_{tb}: timber flexural strength, Z_p: plastic section modulus of the cruciform neck. As shown in Fig. 19, M_p^{r-rest} is evaluated by Equations (23) and (7) for WaL.

3.3. Evaluation of the proposed design methods

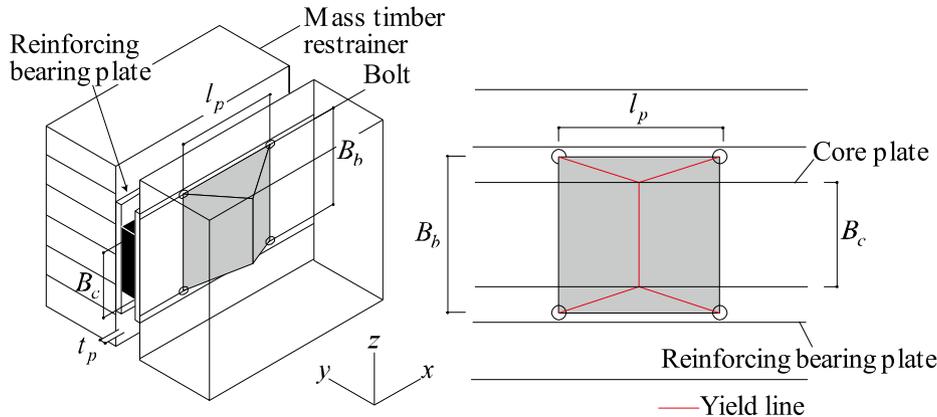The proposed equations were evaluated for each specimen, and the
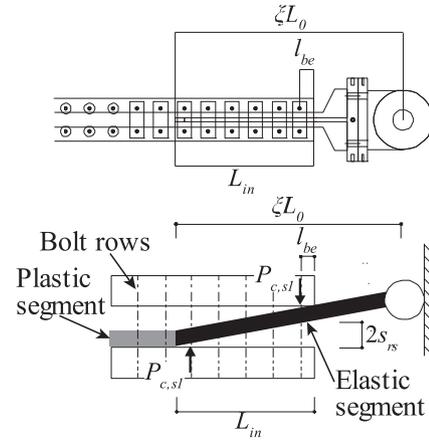

Fig. 19. Failure mode assumption at restrainer-end.

local bulging demand-to-capacity ratios (DCRs) are compared in Table 2 for the Wa and Wb series, and in Table 3 for the Wp series. The global stability DCRs are compared for the long test specimens (WaL, WbL and WpL) in Tables 4 and 5.

1) Bulging of MT-BRBs without side bearing plates (Wa, Wb series)

Table 2 summarizes the bulging DCRs for the specimens lacking side bearing plates (Wa and Wb series). The Wa, Wb, Wa2.5 and Wb2.5 specimens failed in strong-axis bulging, while the Was and Wbs specimens failed in weak-axis bulging. Of those failing in strong-axis bulging, the demand $P_{d,s}$ calculated using the maximum test force N_{max} increased in proportion to the strong-axis debonding gap (Wa and Wb: 1.0 mm, Wa2.5 and Wb2.5: 2.5 mm). The calculated bolt deformation and timber splitting ($P_{c,sl}$) DCRs exceeded 1.0 for Wa and Wb, in agreement with the observed failure modes. The bolt shear ($P_{c,s2}$) DCRs also exceeded 1.0 in most cases, suggesting that the bolts may have yielded had the timber not given way, which agrees with the severe residual deformation of the dismantled bolts.

The Was and Wbs specimens featured larger 0.5 mm weak-axis debonding gaps, and consequently failed in weak-axis bulging. Although the largest DCRs predicted a failure mode of timber bearing at the core wavecrests ($P_{c,w1}$), DCRs for the limit states of timber bearing at the bolt washer ($P_{c,w2}$) and timber bending ($P_{c,w3}$) also exceeded 1.0. These correspond to the observed failure modes, although it should be noted that washer bearing is a contributing factor, rather than sole cause of collapse.

2) Bulging of MT-BRBs with side bearing plates (Wp series)

Fig. 18. Yield line assumption for Reinforcing steel plate.

Table 2
Evaluation of local bulging failure mode (Wa and Wb series, no side plates).

Name	Observed failure mode	Demand		Capacity (per failure mode)									
		Strong-axis	Weak-axis	Strong-axis				Weak-axis					
		Core outward force		Timber splitting with dowel bending		Bolt shear fracture		Timber bearing at core wavecrest		Timber bearing at washer		Timber bending and splitting	
		(at experiment N_{max})											
		$P_{d,s}$ (kN)	$P_{d,w}$ (kN)	$P_{c,s1}$ (kN)	DCR	$P_{c,s2}$ (kN)	DCR	$P_{c,w1}$ (kN)	DCR	$P_{c,w2}$ (kN)	DCR	$P_{c,w3}$ (kN)	DCR
		Eq. (1)	Eq. (2)	Eq. (7)		Eq. (9)		Eq. (10)		Eq. (11)		Eq. (13)	
Wa	Strong-axis bulging (splitting)	15.49	3.55	14.11	1.10	15.09	1.03	8.42	0.42	8.55	0.41	12.55	0.28
Wb	Strong-axis bulging (splitting)	14.92	3.41	14.11	1.06	15.09	0.99	8.42	0.40	21.84	0.16	11.00	0.31
Wa2.5	Strong-axis bulging (splitting)	29.84	3.40	14.11	2.12	15.09	1.98	8.42	0.40	8.55	0.40	12.55	0.27
Wb2.5	Strong-axis bulging (splitting)	28.89	3.28	14.11	2.05	15.09	1.91	8.42	0.39	21.84	0.15	11.00	0.30
Was	Weak-axis bulging (splitting)	11.55	14.24	14.18	0.81	15.09	0.77	8.42	1.69	8.55	1.67	12.55	1.13
Wbs	Weak-axis bulging (splitting)	11.47	14.15	14.18	0.81	15.09	0.76	8.42	1.68	21.84	0.65	11.00	1.29

Min. yield strengh $F = 235$ N/mm²
Timber bending strength, parallel to grain $F_{wb} = 31.2$ N/mm²
Timber bending strength, perpendicular to grain $F_{wbT} = 3.12$ N/mm²
Timber cross-grain bearing strength $F_{wu} = 8.1$ N/mm²

Table 3
Evaluation of local bulging failure mode (WpL, with side plates).

Name	Observed failure mode	Demand		Capacity (per failure mode)											
		Strong-axis	Weak-axis	Strong-axis				Weak-axis							Side bearing plate yielding
		Core outward force		Bolt hole bearing		Bolt shear fracture		Timber bearing at core wavecrest		Timber bearing at washer		Timber bending and splitting			
		(at experiment N_{max})													
		$P_{d,s}$ (kN)	$P_{d,w}$ (kN)	$P_{c,s2-p}$ (kN)	DCR	$P_{c,s2}$ (kN)	DCR	$P_{c,w1-p}$ (kN)	DCR	$P_{c,w2-p}$ (kN)	DCR	$P_{c,w3-p}$ (kN)	DCR	$P_{c,w4-p}$ (kN)	DCR
		Eq. (1)	Eq. (2)	Eq. (14)		Eq. (15)		Eq. (16)		Eq. (17)		Eq. (18)		Eq. (19)	
Wp	Weak-axis bulging (splitting)	13.7	16.1	18.7	0.73	15.1	0.91	15.0	1.08	22.7	0.71	11.5	1.40	16.6	0.97
WpL	Weak-axis bulging (splitting)	13.9	16.4	18.7	0.74	15.1	0.92	15.0	1.09	22.7	0.72	11.5	1.42	16.6	0.99

Min. yield strengh $F = 235$ N/mm²
Timber bending strength, parallel to grain $F_{wb} = 31.2$ N/mm²
Timber bending strength, perpendicular to grain $F_{wbT} = 3.12$ N/mm²
Timber cross-grain bearing strength $F_{wu} = 8.1$ N/mm²

Table 3 summarizes the bulging results for the specimens with side bearing plates (Wp series). Both of the Wp and WpL specimens failed in weak-axis bulging, which agrees with the predicted failure modes. The calculated DCRs for strong-axis bulging were less than 1.0, while the weak-axis bulging DCRs for timber bending ($P_{c,w3-p}$) and side plate bearing ($P_{c,w4-p}$) exceeded 1.0, indicating failure. Furthermore, the large DCR for plate bearing indicates that the side bearing plates were not able to effectively restrain the core, freely transmitting the bulging force to the timber and resulting in the subsequent timber bending failures.

3) Global stability limit including connections

Table 4 summarizes the global stability results for the long specimens (WaL, WbL and WpL). The unreinforced WaL specimen buckled in the first cycle. The improved moment-transfer capacity of the reinforced WbL specimen exceeded the neck axial-flexural strength, increasing the buckling load. The calculated DCRs were in good agreement for WaL, but the capacity was slightly underestimated for WbL. Nevertheless, the experimental results and proposed equations clearly demonstrate the

Table 4
Evaluation of global stability.

Name	Observed failure mode	Insert length (mm)	Connection length (mm)	Maximum axial force (kN)	Global stability			
					Restrainer end moment transfer capacity (kNm)		Buckling capacity (kN)	
		Lin	ξL₀	Ncu	M^r-rest	M^r-neck	Nlim	DCR
					Eq.(23).(24)	Eq.(22)	Eq.(20)	
WaL	Global buckling (restrainer end splitting)	545	378	306.9	2736.9	5325.1	308.1	1.0
WbL	Global buckling (neck yieldimg)	545	378	365.3	2736.9	5325.1	308.1	1.2
WpL	Weak-axis bulging (splitting)	545	378	455.6	14863.5	5325.1	395.6	1.2

Table 5
Global buckling safety factor.

WpL	Core yield force	Compression overstrength factor	Maximum compressive force	Elastic buckling force	Elastic buckling load factor
	N_y (kN)	$_d\alpha$	N_{cu} (kN)	N_{cr}^E(kN)	$_e\alpha(=N_{cr}^E/N_{cu})$
Design	244.4	1.40	342.2	942.5	2.75
Experiment	–	1.86	455.6	–	2.07

Table 6
List of real-size mock-up tests.

Specimen Name	Core plate					Timber restrainer		
	Steel grade	Thick (mm)	Width (mm)	Length (mm)	Yielding Zone (mm)	Grade	Width (mm)	Height (mm)
Wp1000(1000kN)	SN490B	25	130	5370	3750	E95-F315	155	340
Wp1500(1500kN)	SN490B	28	170	5360	3800		170	370
Wp1500A(1500kN)	SN490B	28	170	5360	3800	(Larch)	170	370
Wp2000(2000kN)	SM490A	32	185	7170	5360		210	480

*Min. yield strength $F = 325$ N/mm².
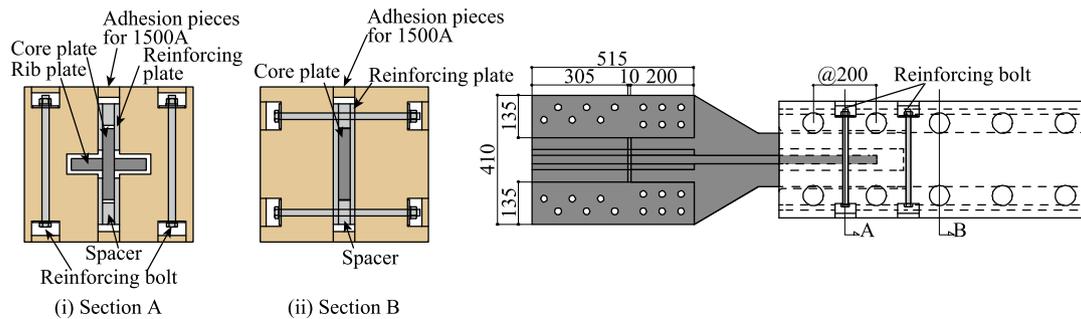
Fig. 20. Section and restrainer-end detail for real-size specimen.

low restrainer-end moment-transfer capacity of MT-BRBs and the particular susceptibility to global buckling when used with pinned connections. While similar vulnerabilities have been noted for conventional pin-ended BRBs [21,22], MT-BRBs differ in that timber limits the restrainer-end moment-transfer capacity, regardless of the provided insert length [15].

4) Overstrength and restrainer design

Table 5 compares the overstrength ratio ($_d\alpha$, alternatively denoted

$\beta\omega$) and elastic buckling factor ($_e\alpha = N_{cr}^E / {_d}\alpha N_y$) of the pinned WpL specimen, with the yield force N_y calculated from the nominal yield strength.

$$N_{cr}^B = \frac{\pi^2 E I_B}{l_B^2} >_e\alpha N_{cu} \qquad (26)$$

$$N_{cu} = {_d}\alpha N_y \qquad (27)$$

where N_{cr}^B is the Euler buckling load of the restraint, E is the timber elastic modulus in bending, I_B is the second moment of inertia of the restrainer and l_B is the effective buckling length, taken as the restrainer length here. The fully-composite I_B was adopted, as this agrees with the initial stiffness obtained from a four point bending test not reported in this paper. However, this is only valid when the frictional resistance between the timber pieces and spacers exceeds the midsection longitudinal shear stress produced as the axial load approaches N_{cr}^B, and so a relatively large elastic buckling factor ($_e\alpha$) may be required to limit these P-Delta demands. Although designed for $_d\alpha = 1.4$ [13], this proved to be less than the experimental overstrength of $_d\alpha = 1.9$ (WpL, 4th cycle at 3% strain). On the other hand, the design adopted an elastic buckling factor of $_e\alpha = 2.8$, significantly exceeding the $1.5 \sim 2.0$ used for conventional BRBs [13], and so the elastic buckling factor remained satisfactory despite the larger experimental overstrength.

4. Full-scale cyclic tests of MT-BRBs

Full-scale MT-BRBs of practical size were designed using the proposed equations, and then fabricated and tested under quasi-static cyclic loading to validate the design method.

4.1. Design of full-scale test specimens

The test specimens' dimensions and materials are depicted in Table 6 and Fig. 20, and are denoted by their nominal yield strengths (1000kN, 1500kN or 2000kN). The Wp1000, Wp1500 and Wp2000 specimens were based on the Wp series with side bearing plates provided to reduce the risk of a brittle bulging failure. The external reinforcing plates at the restrainer end were replaced with bolts, while Wp1500A introduced a further variation of recessed bolts with glued timber cover pieces. The overstrength factors were taken as $_d\alpha = 1.4$ at 2% strain and $_d\alpha = 1.5$ at 3% strain. The demand-to-capacity ratios (DCRs) in Table 7 indicate that weak-axis bulging was critical in each case, but all were safe up to 2% strain, which was adopted as the design strain. Wp1500A was tested beyond the design value up to 3% strain, at which point the weak-axis bulging DCR was predicted to marginally exceed 1.0.

The testing jig and loading protocol are shown in Figs. 21, 22 and 23, respectively. The cantilever connection stability concept was adopted with bolted connections and rigid gusset plates [13,14]. Quasi-static loading with three cycles each at ± 0.1%, 0.5%, 1.0% and 2.0% strain were applied to the Wp1000, Wp1500 and Wp2000 specimens, while Wp1500A was subjected to additional cycles at 3.0% strain. Cycles at the maximum amplitude were then continued until fracture. Prior to the test, both Wp1500 and Wp1500A were laterally offset at one end to simulate a 1% out-of-plane drift, while no offset was applied to Wp1000 and Wp2000.

4.2. Full-scale test specimen results

The hysteresis loops are shown in Fig. 24. Each of the specimens exhibited a stable cyclic response and achieved the desired failure mode of core tensile fracture due to low cycle fatigue. The Wp1000, Wp1500 and Wp2000 specimens fractured after 25, 23 and 23 cycles at 2% strain, while the Wp1500A specimen fractured after 7 cycles at 3% strain. The compression-to-tension ratios (β) were all less than 1.10.

This is reasonably good performance: the design strain and low cycle fatigue capacities were slightly less than conventional BRBs, but still
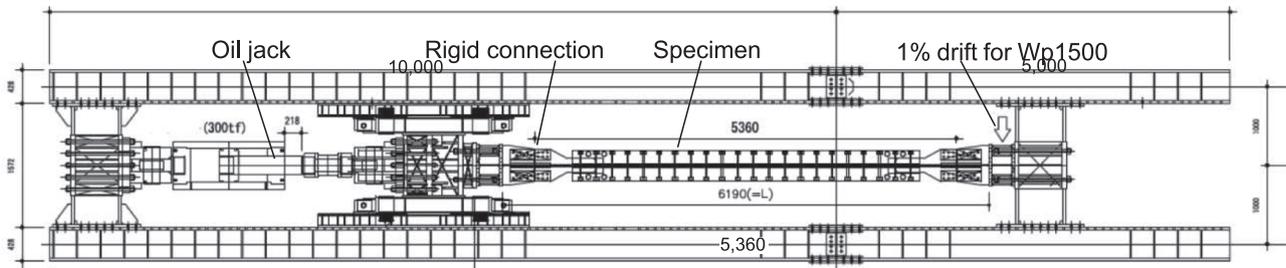
Table 7
Design of full-scale test specimens.

Name	Strain	Observed failure mode	Demand Strong-axis Core outward force (at experiment N_{max}) $P_{d,s}$ (kN) Eq.(1)	Demand Weak-axis $P_{d,w}$ (kN) Eq.(2)	Strong-axis Bolt hole bearing $P_{c,s2p}$ (kN) Eq.(14)	DCR	Strong-axis Bolt shear fracture $P_{c,s2}$ (kN) Eq.(15)	DCR	Weak-axis Timber bearing at core wavecrest $P_{c,s1-p}$ (kN) Eq.(16)	DCR	Timber bearing at washer $P_{c,w2-p}$ (kN) Eq.(17)	DCR	Timber bending and splitting $P_{c,w3-p}$ (kN) Eq.(18)	DCR	Side bearing plate yielding $P_{c,w4p}$ (kN) Eq.(19)	DCR
Wp1000	2%	Core fracture	25.0	35.1	79.9	0.52	48.3	0.31	61.1	0.57	38.0	0.92	43.4	0.81	166.6	0.21
Wp1500	2%	Core fracture	31.4	47.2	130.6	0.40	78.9	0.24	81.7	0.58	51.7	0.91	48.7	0.97	183.3	0.26
Wp2000	2%	Core fracture	37.4	52.9	142.1	0.44	85.9	0.26	94.8	0.56	55.0	0.96	55.4	0.96	189.1	0.28
Wp1500A	3%	Core fracture	44.2	60.5	130.6	0.56	78.9	0.34	81.7	0.74	53.0	1.14	52.4	1.15	183.3	0.33

Bending Standard Strength along grain direction $F_{wb} = 31.2$ N/mm²
Bending Standard Strength perpendicular to grain direction $F_{wbT} = 3.12$ N/mm²
Compressive Standard Strength $F_{wu} = 8.1$ N/mm²

Fig. 21. Plan of test setup.

Fig. 22. Test setup for full-scale MT-BRBs.

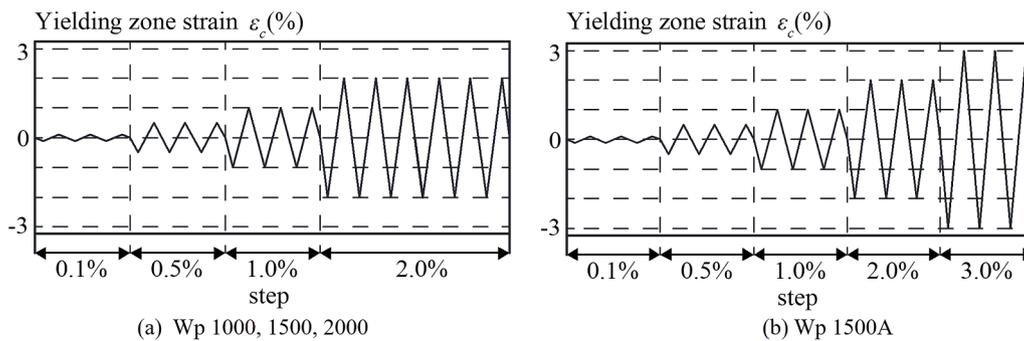(a) Wp 1000, 1500, 2000

(b) Wp 1500A

Fig. 23. Loading protocol.

satisfactory, while the β values were similar. Importantly, the MT-BRBs satisfied the requirements prescribed for conventional BRBs in Japan, permitting their use as ductile, earthquake-resistant braces for low-to-mid rise buildings [13].

5. Conclusions

This study tested mass timber BRBs (MT-BRBs) with different restrainers, steel reinforcing plates, debonding gaps, connections and lengths. Detailed design criteria were proposed for the global stability and bulging failure modes, and validated in successful full-scale tests, with the following findings:

1) MT-BRBs are susceptible to global buckling, but with enhanced restrainer-end details may achieve stable cyclic behavior, ultimately failing in either bulging or the desired low-cycle fatigue core fracture.
2) Bulging was often critical, with strong-axis higher-mode buckling of the core deforming the bolts and splitting the timber, and weak-axis higher-mode buckling causing bearing failures at the core wavecrests or bolt washers, or a timber bending failure. Sandwiching the core with side bearing plates prevented strong-axis bulging and added ductility to weak-axis bulging, but a certain plate thickness is required to be effective.
3) The debonding gap thickness had a strong influence on the deformation capacity and failure mode, and determined the critical direction for bulging. The weak-axis gap was particularly significant, as increasing it from nil to 0.5 mm caused bulging to occur earlier (Wa: 5 cycles vs Was: 3 cycles at 3.0% strain).
4) The timber restrainers exhibited low restrainer-end moment-transfer capacity. Global stability was only attained when reinforcing the restrainer ends with steel plates or employing the "cantilever connection" stability concept with rigid boundary conditions (e.g., bolted connections with stiffened gussets).
5) Causative mechanisms were identified for each failure mode and developed into design methods, which were shown to be in good agreement with the experimental results.
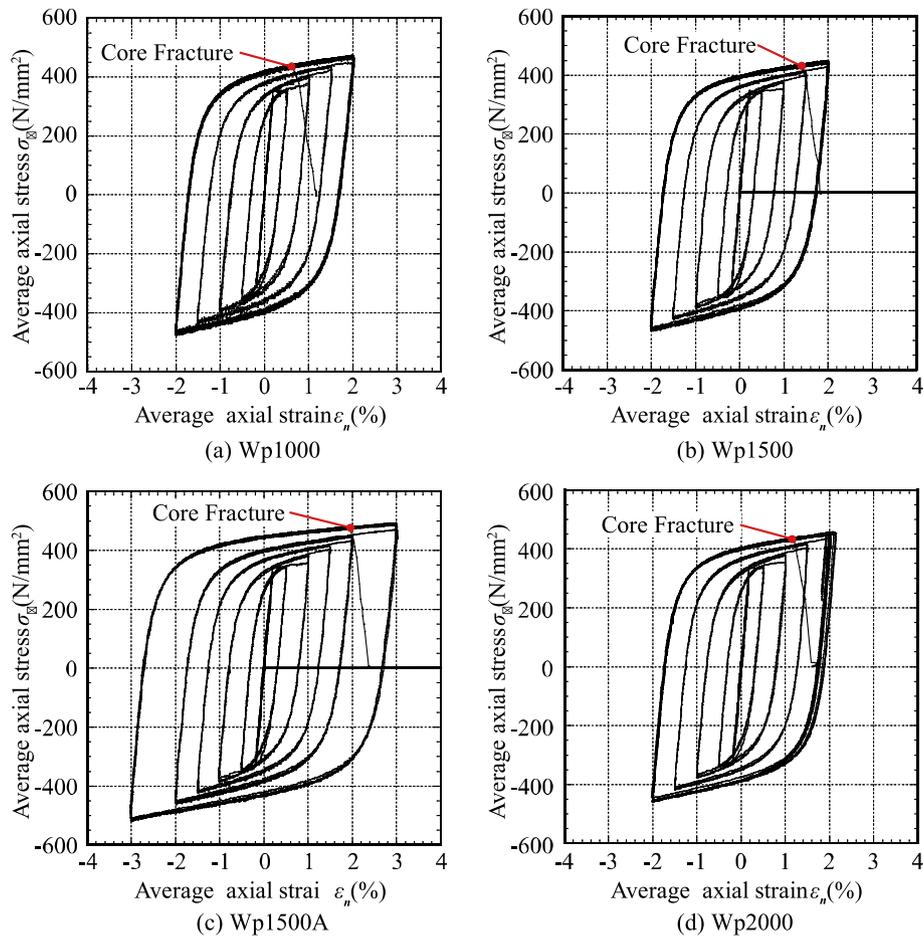
Fig. 24. Hysteresis loops of full-scale MT-BRBs.

6) The proposed design method was applied to 1000-2000kN MT-BRBs, which achieved stable cyclic performance and the desired core tensile facture due to low-cycle fatigue. These full-scale specimens satisfied the performance requirements for conventional BRBs.

7) In general, the authors believe that laminated timber may be employed in BRB restrainers. However, timber increases the risk and consequence of bulging failures, and so steel or hardwood reinforcing plates are highly recommended to ensure a stable and reliable hysteresis.

Nevertheless, it should be noted this is just one test series and further research may be required to confirm the general validity of the proposed design method. Also, the brittle failure modes, exposure of the debonding gap to the dimensional stability of the timber and reliance on composite action of the bolted timber may justify a greater degree of conservatism for MT-BRBs than conventional BRBs.

Credit authorship contribution statement

Toru Takeuchi: Supervision, Conceptualization, Investigation, Writing – review. **Yuki Terazawa:** Supervision, Investigation, Formal analysis, Writing – review. **Shogo Komuro:** Investigation, Visualization. **Takashi Kurata:** Conceptualization, Investigation. **Ben Sitler:** Formal analysis, Edit – review.

Declaration of Competing Interest

The authors declare that they have no known competing financial interests or personal relationships that could have appeared to influence the work reported in this paper.

References

[1] Quintana Gallo P, Carradine DM, Bazaez R. State of the art and practice of seismic-resistant hybrid timber structures. Eur J Wood Wood Prod 2021;79(1):5–28.
[2] Li Z, Dong H, Wang X, He M. Experimental and numerical investigations into seismic performance of timber-steel hybrid structure with supplemental dampers. Eng Struct 2017;151(15):33–43.
[3] Anil C, Gohlich R, Erochko J, Woods JE. Experimental testing and numerical modelling of a heavy timber moment-resisting frame with ductile steel links. Earthquake Eng Struct Dyn 2018;47(6):1460–77.
[4] Harada H, Saito R, Nakajima S, Yamazaki Y, Terazawa Y, Hayashi K, et al. Cyclic elasto-plastic deformation capacity of dog bone timber-steel hybrid connections. Transactions of AIJ 2020;85(773):945–55.
[5] Dong W, Li M, Lee C-L, MacRae G, Abu A. Experimental testing of full-scale glulam frames with buckling restrained braces. Eng Struct 2020;222:111081.
[6] Yamada S, Kishiki S. A study on stiffening efficiency of Buckling-restrained Braces (Part 1. Efficiency of wooden retraint), AIJ annual conference, 2014. (in Japanese).
[7] Blomgren HE, Koppitz JP, Diaz, Valdes A. and Ko E. The heavy timber buckling-restrained braced frame as a solution for commercial buildings in regions with high seismicity: Performance of column and beams, Proceedings of 14th WCTE, pp.3515-3524, 2016.8.
[8] Resta J. The timber buckling restrained brace frame. San Luis Obispo: California Polytechnic State University; 2019.
[9] Murphy C, Pantelides CP, Blomgren HE, Rammer D. Development of timber buckling restrained brace for mass timber-braced frames. Journal of Structural Engineering, ASCE 2021;147(5):5.

[10] Yamamoto Y, Yoshida F. and Nakagawa M. Cyclic loading test of buckling restrained brace using wood material (Parts 1 and 2), Summaries of Technical Papers of Annual Meeting, Architectural Institute of Japan, pp. 741-744, 2018.7 (in Japanese).

[11] Yoshida F, Nakagawa M, Yabuta T, Nishi T, Abeyama T. Cyclic loading test of buckling restrained brace using laminated wood (Parts 1 and 2), Summaries of Technical Papers of Annual Meeting, Architectural Institute of Japan, pp. 995-998, 2019.7 (in Japanese).

[12] Haga Y, Taguchi T, Shimizu K, Kondo T. and Kato M. Development of the buckling-restrained steel-plate braces using glued laminated timber, (Part 1 to Part 3), Summaries of Technical Papers of Annual Meeting, Architectural Institute of Japan, pp. 1535-1540, 2019. 7 (in Japanese).

[13] Takeuchi T, Wada A. Buckling-restrained braces and applications. JSSI 2017.

[14] AIJ: Recommendation for stability design of steel structures, 2018 (in Japanese).

[15] Takeuchi T, Ozaki H, Matsui R, Sutcu F. Out-of-plane stability of buckling-restrained braces including moment transfer capacity. Earthquake Eng Struct Dyn 2013.10.;43(6):851–69.

[16] Takeuchi T, Hajjar JF, Matsui R, Nishimoto K, Aiken ID. Local buckling restraint condition for core plates in buckling restrained braces. J Constr Steel Res 2010;66 (2):139–49.

[17] Lin P-C, Tsai K-C, Chang C-A, Hsiao Y-Y, Wu A-C. Seismic design and testing of buckling-restrained braces with a thin profile. Earthquake Eng Struct Dyn 2016;45 (3):339–58.

[18] Dehghani M, Tremblay R. An analytical model for estimating restrainer design forces in bolted buckling-restrained braces. J Constr Steel Res 2017;138:608–20.

[19] Kamachi K, Inayama M, Ando N. Design method to estimate the load-slip characteristics of bolted or drift-pinned joints with the steel inserted plate. Nihon Kenchiku Gakkai Kozokei Ronbunshu 2008;73(627):795–802.

[20] AIJ: Fundamental theory of timber engineering, 2010.

[21] Jiang ZQ, Dou C, Guo YL, Zhang AL. End detailing experimental study of the pinned double-rectangular tube assembled buckling-restrained brace [J]. J Constr Steel Res 2017;133:334–44.

[22] Jiang ZQ, Dou C, Guo YL, Zhang AL. Theoretical study on design methods for pinned assembled BRB with flat core [J]. Eng Struct 2017;133:1–13.